SOME SIGMOID AND REVERSE-SIGMOID RESPONSE PATTERNS EMERGING FROM HIGH-POWER LOADING OF SOLIDS

Sreten Mastilović

ABSTRACT. The objective of the present review is twofold. First, it aims at highlighting some sigmoid and reverse-sigmoid response patterns observed recently in the course of simulations of the high-strain-rate loading of (mostly, quasibrittle) solids. Second, it aims at reviewing various properties of two models used frequently as curve fitting tools for nonlinear and saturable phenomena. These two models-inspired by the Hill and the Weibull cumulative distribution functions-are bounded by two horizontal asymptotes with a smooth transition between the baseline and the final saturation state, characterized by a non-negative (a non-positive) derivative at each point for the sigmoid (the reverse-sigmoid) shape. Although they were used primarily for data fitting because of their flexibility and effectiveness, these nonlinear models possess other properties useful for the analysis of the irreversible, nonlinear and far-from-equilibrium phenomena. The main features of these two models are systematically examined in this review. In spite of the fact that satisfactory curve-fitting of data could not be considered a proof of causality it could underline a pattern of behavior and, perhaps, provide an investigation guidance.

1. Introduction

The deformation and failure of materials subjected to extreme loading powers are of increasing interest in physics and engineering. The experience suggest that the heterogeneous material texture usually exerts a strong influence on the performance of materials subjected to such loading conditions, which is especially true in the case of quasibrittle materials characterized additionally by an inferior cohesive strength. Research efforts towards modeling of materials prone to microcracking, spanning most of the last century, suggest that a rational model should be based on the statistics of the weak links and hot spots. This invokes readily the Weibull distribution, a prominent member of the family of extreme value distributions [1].

On the other hand, recent numerical simulations (e.g., [2, 3]) indicate that the effect of sample size on strength eventually decreases with increasing strain rate and becomes practically negligible at ultrahigh strain rates as the dynamic response of a solid becomes more deterministic and less affected by stochasticity of its texture.

Despite ever-increasing capabilities of experimental-mechanics techniques, the range of strain rates and shear strains achievable in high-strain-rate experiments (most notably, the impact experiments) leaves a lot to be desired. As an example, the experimental data recorded during ballistic tests is more often than not limited to the projectile velocity, penetration depth, debris cloud shape, and *a posteriori* observation of projectile fragments and the crater. On the contrary, the computer experiments, such as the pair presented in this review, offer almost unlimited control over the "virtual testing". Their often-advertised ability to probe regions beyond current experimental limits and offer insights into otherwise inaccessible details seems limited only by quality of the physical model, computer capabilities (remarkably growing though never sufficient), corresponding advance of numerical algorithms, and ingenuity of researchers.

The sigmoid and reverse-sigmoid patterns of the dynamic-response data presented herein are examples of the simulation results obtained by two prominent techniques of computational mechanics of discontinua: molecular dynamics and lattice method. The common features of these neat and complex data patterns are their nonlinear and saturable character that appears to arise quite naturally from the high-strain-rate loading of the disordered material with random microstructure. Consequently, two different deterministic models are examined in this article

$$(1.1a) \qquad \bar{y} = \bar{y}_0 + (\bar{y}_1 - \bar{y}_0)\frac{(x-A)^\alpha}{H^\alpha + (x-A)^\alpha}, \qquad x > A$$

$$(1.1b) \qquad \bar{y} = \bar{y}_0 + (\bar{y}_1 - \bar{y}_0)\Big\{1 - \exp\Big[-\Big(\frac{x-A}{B}\Big)^\alpha\Big]\Big\}, \qquad x > A$$

and referred to as the Hill model and the Weibull model, respectively. They share the same advantages of being flexible and effective in fitting the simulation data characterized by a smooth transition with a single-sign gradient (either non-negative or non-positive) between two horizontal asymptotes ($\bar{y}_0$ and $\bar{y}_1$) corresponding to the lower and upper domain boundaries of the independent variable. The bar above symbols is used to emphasize the normalized variables ($0 < \bar{y} = y/y_{\max} < 1$) used throughout this article. Admittedly, a variety of relationships can be found that provide similarly effective data fit. Although the satisfactory curve-fitting of data cannot be considered a proof of causality it is hoped that it might underline a pattern of behavior and that a repeated occurrence of the same pattern may provide some investigation guidance. Thus, the model parameter values are often formally informative although without providing insights into the mechanisms involved in any specific case to be discussed. Specifically, two parameters designated by lowercase Greek letters (α, β), which may reflect heterogeneity in the response, are commonly referred to as the shape (or sigmoidicity) coefficients; H, which may indicate the affinity or sensitivity of the system or both, is called the location parameter; and A and B are the translation parameter and the scale parameter, respectively.

2. Some descriptive and probabilistic properties
of the selected curve-fitting models

Equations (1.1) belong to the category of deterministic or pseudo-deterministic models because-assuming they correctly describe a particular response feature-once the model parameters are estimated, they are able to predict the system behavior outside the domain used for the parameter estimation; or, it is hoped, the system behavior under similar conditions. The effect of the modeling can, depending on a particular observed pattern of behavior, capture either monotonically increasing (sigmoid) or decreasing (reverse-sigmoid) dependent variable with increasing independent variable. Thus, the descriptive properties of equations (1.1) have been used extensively for curve-fitting of experimental and simulation data that exhibit such nonlinear and saturable character. It is important to note that equation (1.1b) is inspired by the translated (three-point) Weibull cumulative distribution function:

$$(2.1) \qquad F(x \mid \beta, \eta, \gamma) = 1 - \exp\left[-\left(\frac{x-\gamma}{\eta}\right)^{\beta}\right]; \qquad x \geqslant \gamma, \ \gamma \in \Re, \ \beta, \eta \in \Re^{+}$$

that exhibits the desired sigmoid shape with γ, η and β being the location, scale, and shape parameters, respectively, such that $(-\infty < \gamma < \infty)$, $\eta > 0$, and $\beta > 0$. The related probability density function is

$$(2.2) \ \ f(x \mid \beta, \eta, \gamma) = \frac{\beta}{\eta}\left(\frac{x-\gamma}{\eta}\right)^{\beta-1}\exp\left[-\left(\frac{x-\gamma}{\eta}\right)^{\beta}\right]; \quad x \geqslant \gamma, \ \gamma \in \Re, \ \beta, \eta \in \Re^{+}.$$

The Weibull distribution is widely applied to many random phenomena due to its extreme value behavior (e.g., [4])[1]. The appropriate selection of distribution parameters allows close approximation of many observational phenomena. The median, one of commonly used measures of central tendency of the data sample, in the case of the translated (3-point) Weibull distribution has the form:

$$(2.3) \qquad\qquad\qquad M = \gamma + \eta(\ln 2)^{1/\beta}.$$

The two-parameter Weibull distribution, commonly used in reliability engineering, is a special case of the translated Weibull distribution (2.1) with $\gamma = 0$. It corresponds to the generalized extreme value distribution when the shape parameter is replaced: $-\beta \to \beta$ (the Frechet distribution). Equation (1.1a), extensively used in various branches of biosciences [6], corresponds to the translated Hill cumulative distribution function

$$(2.4) \qquad F(x \mid \beta, \zeta, \varsigma) = \frac{(x-\varsigma)^{\alpha}}{\zeta^{\alpha} + (x-\varsigma)^{\alpha}}; \qquad x \geqslant \varsigma, \ \varsigma \in \Re, \ \alpha, \zeta \in \Re^{+}.$$

Equation (2.4) has been applied in many forms to describe probabilistic aspects of various nonlinear and saturable relationships [7].

The corresponding probability density function is

$$(2.5) \qquad f(x \mid \beta, \zeta, \varsigma) = \frac{\alpha\zeta^{\alpha}(x-\varsigma)^{\alpha-1}}{[\zeta^{\alpha} + (x-\varsigma)^{\alpha}]^{2}}; \qquad x \geqslant \varsigma, \ \varsigma \in \Re, \ \alpha, \zeta \in \Re^{+},$$

---

[1]The Weibull-type distribution was, apparently, first applied in engineering practice by Rosin and Rammler [5] to describe particle size distribution.

while the median of the translated Hill distribution has the form:

(2.6) $$M = \zeta + \varsigma.$$

Consequently, in view of equations (2.1) through (2.6), it is sometimes convenient to rewrite equations (1.1) in the forms

(2.7a) $$\bar{y} = \bar{y}_0 + (\bar{y}_1 - \bar{y}_0)\frac{(x - A)^\alpha}{(x_{0.5} - A)^\alpha + (x - A)^\alpha}, \qquad x > A,$$

(2.7b) $$\bar{y} = \bar{y}_0 + (\bar{y}_1 - \bar{y}_0)\left\{1 - \exp\left[-\ln(2)\cdot\left(\frac{x - A}{x_{0.5} - A}\right)^\beta\right]\right\}, \qquad x > A,$$

that emphasize the central tendency by the parameters $x_{0.5}$ which represent the value of the independent variable corresponding to the value of dependent variable $\bar{y}_{0.5} = (\bar{y}_0 + \bar{y}_1)/2$ (the fifth quantile).

The effect of these parameters is illustrated in Figure 1 for sigmoid-type curves; the extension to reverse-sigmoid curves is straightforward. Because of their flexibility, these models were used primarily as curve fitting tools and their many other interesting aspects and properties were, if not overlooked than, not systematically examined.
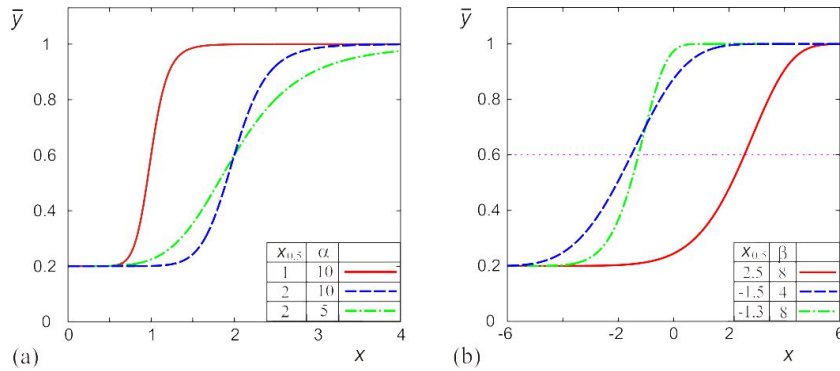

FIGURE 1. Examples of sigmoid type of the Hill (a) and Weibull (b) models normalized to $\bar{y}_1 = 1$ and with the same baseline value $\bar{y}_0 = 0.2$ but different translation parameter values $A = 0$ and $A = -7$, respectively. The remaining parameter values are given in the figure inset tables. Note that the negative values of the shape parameter α directly yield the reverse-sigmoid shape.

First, with regards to the mathematical and graphical properties, the plots in Figure 1 corresponding to equations (2.7)

$$\tilde{x} = \left(\frac{\alpha - 1}{\alpha + 1}\right)^{1/\alpha}(x_{0.5} - A)$$

$$\tilde{x} = A + \left(\frac{\beta - 1}{\ln(2)\beta}\right)^{1/\beta}(x_{0.5} - A),$$

calculated in usual manner by using the condition that the second derivative has an isolated zero and a sign change.

The slope of the sigmoid curve at the inflection point

$$(2.8a) \qquad \tilde{y}' = \bar{y}'(x = \tilde{x}) = \frac{\alpha^2 - 1}{4\alpha}\left[\left(\frac{\alpha - 1}{\alpha + 1}\right)^{1/\alpha}(x_{0.5} - A)\right]^{-1}(\bar{y}_1 - \bar{y}_0)$$

$$(2.8b) \quad \tilde{y}' = \bar{y}'(x = \tilde{x}) = [\ln(2)]^{1/\beta}\beta\omega^\omega \exp(-\omega)(x_{0.5} - A)^{-1}(\bar{y}_1 - \bar{y}_0), \quad \omega = \frac{\beta - 1}{\beta}$$

is an informative parameter defined as the maximum gradient of the dependent variable change.

Second, with regards to the probabilistic aspects, equations (2.7) may be used as probabilistic expressions in light of expressions (2.1)–(2.6). An immediate benefit of that analogy is to use quantiles for the fitting purpose. The calculation of different quantiles is straightforward knowing a cumulative distribution function, $F(x)$. A quantile x_q of the distribution function $F(x)$ is the solution of the equation $F(x_q) = q$ with $0 < q < 1$. In case of monotonically increasing functions, such as the sigmoid functions defined by (1.1), the quantiles are singles

$$(2.9a) \qquad x_q = A + \left(\frac{q}{1 - q}\right)^{1/\alpha}H$$

$$(2.9b) \qquad x_q = A + \left[\ln\left(\frac{q}{1 - q}\right)\right]^{1/\beta}B$$

With regards to equations (2.9), for the symmetric quantiles x_q and x_{1-q}, it is straightforward to derive the ratios

$$(2.10a) \qquad \frac{x_q - A}{x_{1-q} - A} = \left(\frac{q}{1 - q}\right)^{2/\alpha}$$

$$(2.10b) \qquad \frac{x_q - A}{x_{1-q} - A} = \left\{\frac{\ln[1/(1 - q)]}{\ln(1/q)}\right\}^{1/\beta}$$

which for the particular choice of quantiles, depend only on the shape and translation model parameters. Thus, based on equations (2.10), it is a simple exercise to derive the general relationships

$$(2.11a) \qquad \alpha = 2 \cdot \frac{\ln\left(\frac{q}{1-q}\right)}{\ln\left(\frac{x_q - A}{x_{1-q} - A}\right)}$$

$$(2.11b) \qquad \beta = \frac{\ln\left(\frac{\ln[1/(1-q)]}{\ln(1/q)}\right)}{\ln\left(\frac{x_q - A}{x_{1-q} - A}\right)}$$

between the sigmoidicity (shape) coefficients α and β of the Hill equation and the Weibull equation, respectively, and the corresponding symmetric quantiles x_q and x_{1-q}. Equations (2.11) permit calculation of the parameters α and β if the quantiles can be estimated based on available data. This is especially convenient

if the observed process is not fully developed and/or the asymptotic approach to final saturation state is not reached.

Finally, with symmetric quantiles known and sigmoidicity coefficients determined (2.11), simple expressions

$$(2.12a) \qquad\qquad H = \sqrt{(x_q - A)(x_{1-q} - A)}$$

$$(2.12b) \qquad\qquad B = \sqrt{\frac{(x_q - A)}{[\ln(1/q)]^{1/\beta}} \frac{(x_{1-q} - A)}{[\ln(1/(1-q))]^{1/\beta}}}$$

permit calculations of the parameters H and B of the Hill model (1.1a) and the Weibull model (1.1b), respectively.

3. Computer Simulation Methods

The simulation techniques used to obtain results presented in this review article are only succinctly summarized for the sake of completeness. These methods of computational mechanics of discontinua were, among others, recently discussed in references [8] and [9]. The dynamic response patterns reviewed herein were obtained by use of physical models that were, admittedly, rather rudimentary. This was necessitated, if not fully justified, by a number of reasons. First, the limited objective to capture *qualitatively* the salient features of the investigated phenomena. Second, these phenomena are inherently extremely demanding computationally. Last but not least, the capabilities of hardware available to the author leave *a lot* to be desired.

3.1. Molecular Dynamics. MD is a convenient tool to investigate dynamic response of solids under extreme loading conditions by high-resolution virtual testing. Therefore, it frequently assumes a role of a "computational microscope" to explore evolution of discrete systems at spatial and temporal scales that go beyond the current experimental limits (e.g., [3,10–12]). The present approach is limited to the classic MD simulation technique in which the dynamic state of an atomic system is defined by laws of Newtonian mechanics with atomic motions being uniquely determined by empirical potentials. Thus, a monatomic system (mimicking a monocrystalline sample) is comprised of atoms of equal masses $m_I = m_0$ $(I = 1, N_{at})$ that form an ideal triangular lattice and interact with their nearest neighbors according to the L-J (Lennard–Jones) potential. The Cauchy problem is solved numerically by using the Verlet algorithm and the neighbor-list method [9,13,14] with the time step as low as a fraction of femtosecond [11,12]. The extremely small time step, necessitated by the ultrahigh power of the simulated events, makes the simulations painstakingly time-consuming even for the relatively small model size. The simulations generate information at the nanoscale level: atomic positions and velocities, and interatomic forces. The conversion of these information to macroscopic observables such as temperature, stress and strain requires theories developed in the realm of statistical mechanics (e.g., [15, 17] and references therein). Succinctly, the components of the mechanical stress tensor and effective stiffness tensor at the scale of small sets of atoms are

$$(3.1a) \qquad \sigma_{ij} = \frac{1}{2\Omega} \sum_{\substack{I,J \\ J \neq I}} \frac{(r_{IJ})_i (r_{IJ})_j}{|r_{IJ}|} \frac{d\varphi(r_{IJ})}{dr_{IJ}},$$

$$(3.1b) \qquad C_{ijkl} = \frac{1}{2\Omega} \sum_{\substack{I,J \\ J \neq I}} \left\{ \frac{d^2\varphi(r_{IJ})}{dr_{IJ}^2} - \frac{1}{r_{IJ}} \frac{d\varphi(r_{IJ})}{dr_{IJ}} \right\} \frac{(r_{IJ})_i (r_{IJ})_j (r_{IJ})_k (r_{IJ})_l}{|r_{IJ}|^2}$$

where $\varphi(r_{IJ})$ is L-J 6-12 pairwise interatomic potential, $(r_{IJ})_i$ is the i-component of the vector r_{IJ}, and Ω the "volume" of evaluation (averaging) regions[2]. Zhou [15] demonstrated that the stress expression based on interatomic force term alone (3.1a) is a valid mechanical stress measure identifiable with the Cauchy stress. It should be noted that the mechanical stress and effective stiffness, defined by interatomic forces and atomic positions (3.1), become physically ill-defined when the averaging area, in the course of severe distortion or fragmentation, becomes incompletely occupied by atoms. Finally, two-dimensional triangular lattice is equivalent to three-dimensional continuum under plane-strain conditions [16]. Thus, expression for the modulus of elasticity and Poisson's ratio

$$(3.2) \qquad E = \frac{C_{1212}(3C_{1111} - 4C_{1212})}{C_{1111} - C_{1212}}, \quad v = \frac{C_{1111} - 2C_{1212}}{2(C_{1111} - C_{1212})}$$

of isotropic material in terms of two arbitrary stiffness components follow from the plane strain relations. The strain components can be calculated straightforwardly by comparing lattice configurations in the current and initial (reference) states. The components of the left Cauchy-Green strain tensor (notation and terminology adopted from Buehler [17]) of atom I in two-dimensional systems are commonly defined by

$$(3.3) \qquad b_{ij} = \sum_{J} \frac{(r_{IJ})_i (r_{IJ})_j}{3r_0^2}$$

where summation is performed over J nearest neighbors, and r_0 denotes the equilibrium interatomic distance. The other strain measures can be obtained from equation (3.3) (e.g., [17]). It cannot be overemphasized that, unlike the stress counterpart (3.1a), the virial strain (3.3) is valid instantaneously in time and space [3].

After protracted period of reflections upon the physical meaning of thermodynamic temperature under the extreme loading conditions, the consensus was reached within the research community that the appropriate measure should be based on the Gibbs' temperature definition, familiar from the kinetic theory

$$(3.4) \qquad T_I = \frac{1}{2N_I k_B} \sum_{J=1}^{N_I} m_J (v_{xJ}^2 + v_{yJ}^2), \qquad I = 1, \ldots, N_{at}$$

where k_B is the Boltzmann's constant, v_x and v_y are the vibrational velocity components for two-dimensional problems, and averaging is performed over N_I atoms belonging to an averaging area centered at atom I [18]. The instantaneous kinetic

---

[2]Note that the capital alphabetic indices refer to particular atom, while the small alphabetic indices are reserved for tensor components.

temperature (3.4), related to the point of space centered at atom I, is averaged in both space and time (in accordance with the ergodic hypothesis). The averaging area is commonly assumed to be either the whole sample or the local regions mimicking the measurement gages [11]. Note that:

    i) the total velocity follows directly from the solution of Newton's equations of motion,

    ii) the velocity of correlative motion ("systematic" in Fung's [19] terminology) is obtained as the spatial average of total velocities of all atoms belonging to an averaging area, while

    iii) the vibrational ("random", [19, p. 4]) velocity components used in (3.4) are obtained by subtracting the velocity of correlative motion from the total particle velocity [11].

The temperature definition (3.4) has the firm statistical-mechanics foundations since it follows from the canonical ensemble maximum-probability distribution. It was verified by the statistical hypothesis testing that the vibrational velocities obtained from these MD simulations represent a random sample corresponding to the Maxwell–Boltzmann distribution [12]. The temperature evolution in time and space can be vividly presented with a very high-resolution [11].

3.2. Lattice model. The lattice (spring network) method is an engineering offshoot of MD born of the current computational limitation of MD systems to ensembles of $\approx 10^{12}$ atoms. This method of computational mechanics of discontinua appears custom made for brittle multiphase materials that contain hard interior domains (aggregates, grains, granules, etc.) embedded within an inferior-stiffness matrix. It was used extensively in the past to investigate stochastic damage evolution in low-fracture energy systems (e.g., [2, 3, 20]). Computational domain is defined as a collection of "continuum particles" [21, p. 4]. These microphysical objects are envisioned as conglomerates of atoms small enough to consider macroscopic tractions on its external boundaries to be uniform, and large enough to be statistically homogeneous. In short, the mesoscale sample is approximated by an idealized two-dimensional structure: a Delaunay simplical graph dual to a Voronoi froth representing, for example, abovementioned hard interior domains. In general, the identification of the microconstituent that dominates the macroresponse is a problem-specific task. As an example, if the considered quasibrittle material is a polycrystalline ceramics, it is often justified to assume, within this simulation framework, that investigation objectives are met by the following model features:

    i) the direct first-order effects on the overall dynamic response are provided by the glassy grain boundaries ("the most common examples of weak interfaces in brittle materials" [22]);

    ii) the model resolution length, l_c, is defined by the average grain facet size;

    iii) the stiffness and strength distributions account for other mesoscale heterogeneities and defects, such as pores or poorly bound interfaces, which result in local stress and strain fluctuations [1].

Thus, the two-dimensional microstructural texture is represented by a network of one-dimensional elements mimicking inferior-strength grain boundaries (or

interfaces) and, consequently, the dominant damage mechanism is intergranular cracking.

The particles located in lattice nodes interact with their nearest neighbors through the nonlinear central-force links. In the studies whose results are presented henceforth, the interparticular forces stem from a hybrid potential consisting of the Hook potential in tension and the Born–Meyer potential in compression. The simulation model incorporates both aleatory variability and epistemic uncertainty in a straightforward manner. The randomness of the lattice morphology is defined by the coordination number z and link length λ (the counterpart of the interatomic distance r in MD). The lattice is geometrically and structurally disordered since the equilibrium distances between particles and their mutual link stiffness are sampled from their respective distributions within the range $(\alpha_\Lambda \bar{\lambda}) \leqslant \lambda \leqslant [(2 - \alpha_\Lambda)\bar{\lambda}]$ and $(\beta_\Lambda \bar{k}) \leqslant k \leqslant [(2 - \beta_\Lambda)\bar{k}]$. The order parameters, α_Λ and β_Λ define bandwidth of the geometrical disorder and stiffness distribution, respectively [20]. This inherent randomness of the material texture is further enhanced by the nucleation-dominated damage evolution governed by the local fluctuations of stress and energy quenched barriers. The rupture criterion of the link between bulk particles I and J is in the present simulation set defined in terms of the critical elongation $\varepsilon_{IJ} = \Delta\lambda_{IJ}/\lambda_{0IJ} = \varepsilon_{cr} = \text{const}$.

The disordered-lattice simulations replicate rather well the underlining phenomenology of the sample response including the essential features of rate-dependent fracture and deterioration of the effective stiffness, and provide an elementary intuition on the phenomena [23]. Consequently, in spite of the recognized limitations and drawbacks of this rudimentary physical model (examined, for example, in [3] and references therein), these simulations prove a useful tool for qualitative analysis of universal trends of the dynamic behavior of quasibrittle materials and provide a priceless guide for derivation of rational models (e.g., [8, 31]).

4. Simulation Setups and Observations

Two curve-fitting expressions (2.7) are used in this section to describe various response parameters in three different experimental settings. These dynamic tests were simulated by MD and lattice techniques briefly summarized in the preceding section. The sigmoid and reverse-sigmoid response patterns were observed in widely different macroscopic observables and state variables. In this section three different simulation setups of:

 (i) the dynamic uniaxial tension,
 (ii) the dynamic hole expansion, and
 (iii) the ballistic Taylor test are presented.

The display focus is on their nonlinear and saturable response patterns, which are than discussed in view of the two phenomenological models presented in Section 2.

4.1. Dynamic Uniaxial Tension. The uniaxial tension test is the most frequently used experiment in the characterization of engineering materials primarily due to the relatively simple apparatus and rapid execution. It has been suggested repeatedly, though, that the interpretation of its results may not be as simple as it

might appear at first sight, as vividly argued by the Orowan's memorable pocket-watch analogy [24, p. 70]. In the present lattice simulation setup, a square notch-free sample of size L was loaded by uniformly distributed tensile load of strain rate, $\dot{\varepsilon}$ (see Inset (A) of Figure 2). The problem of the uniform load distribution under the extremely high loading rates was resolved by imposing an instantaneous initial velocity field to the lattice in the loading direction, $\dot{x}_1(t=0) = \dot{\varepsilon}x_1$, and perpendicular to it, $\dot{x}_2(t=0) = -v_0^{(\varepsilon)}\dot{\varepsilon}x_2$ (defined in terms of the prescribed strain rate $\dot{\varepsilon} = \dot{L}/L$). This modeling approach was inspired by the Holian and Grady's adiabatic expansion setup [25] widely used subsequently in dynamic simulations. The details of the loading procedure and corresponding effects of the model response were described in [20]. The tensile-test simulations were performed at 13 different strain rates. The maximum stress achieved in the loading direction was identified with the tensile strength and depicted by circles in Figure 2 versus the strain rate. Notably, the solid symbols represent the mean strength obtained from 30 different statistical realizations at the five selected strain rates. On the other hand, the eight hollow circles mark the results of only a single realization per strain rate. This work-load reduction was necessitated by the demands of computational economy. For the same reason, only a single realization was performed for eight different lattice sizes, selected over the wide range from $L/l_c = 9$ to $L/l_c = 765$. Notably, this selection fulfilled the requirement that "the RVE (representative volume element) must be several orders of magnitude larger than the size of its microconstituents" [26]. The used reduced-units geometric and structural lattice parameters were: the bulk coordination number $z = 6$, the average equilibrium distance between particle sites $\bar{\lambda} = l_c = 1$, the average link stiffness $\bar{k} = 50$, the geometrical-order parameter $\alpha_\Lambda = 1/5$, the structural-order parameter $\beta_\Lambda = 2/3$ and the rupture strain of the links $\varepsilon_{cr} = 0.35\%$ [3].

4.1.1. *Tensile strength dependence on the strain rate.* As previously noted, the tensile strength is identified herein with the maximum stress value corresponding to the critical point – the peak of the stress-strain curve that separates the hardening from the softening response. (All properties corresponding to this critical point are marked henceforth with the subscript "m".) It is well established nowadays that the ultimate tensile strength of quasibrittle materials is a rate-dependent stochastic property (e.g., [27]), which, as a rule, exhibits a remarkable extrinsic size effect. Figure 2 illustrates the rapid hardening of the brittle response with the rate increase, various aspects of which were discussed in detail in [2, 3, 20, 27]. A remarkable feature of this virtual testing was that it was performed under the identical loading conditions for a broad strain-rate range. In actual physical experiments, this range is commonly covered by widely different test setups starting from the conventional cross head devices (the quasistatic loading with practically negligible inertia; $\dot{\varepsilon} \leqslant 10\,\text{s}^{-1}$) to the plate impact devices (dominated by inertia to the extent that 1D stress is impossible; $\dot{\varepsilon} \leqslant 1 \cdot 10^8\,\text{s}^{-1}$)

The lattice simulations indicate that the increase of the loading rate results in increase of the mean tensile strength, limited by the two horizontal asymptotes (σ_{m0} and σ_m^{th}) that are, respectively, strongly and negligibly dependent on the system disorder [3]. This loading rate increase has trends towards:
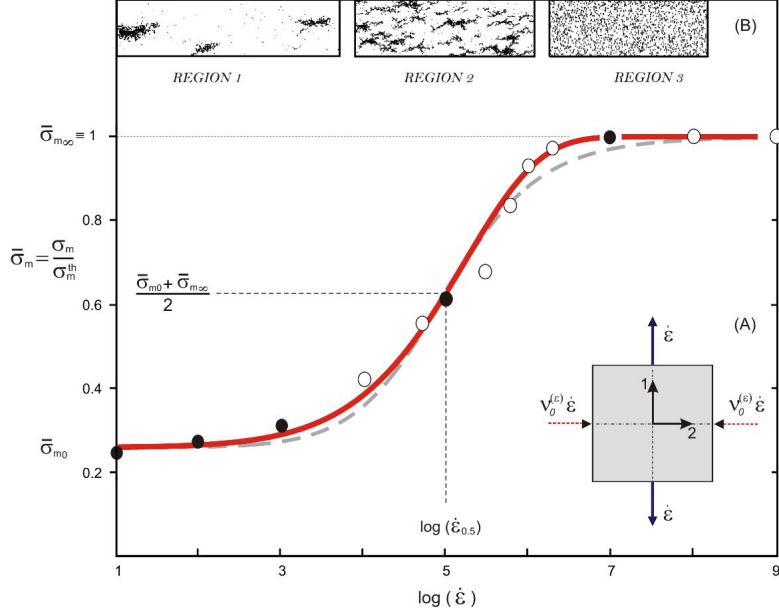
FIGURE 2. Mean tensile strength vs. strain rate. The solid circle represents the mean strength obtained from 30 different statistical realizations at the five selected strain rates while the hollow circles depict one single realization at eight additional strain rates [2]. The dashed (gray) line and the solid (red) line represent data fits obtained by using Equations (2.7a) and (2.7b)) with sigmoidicity coefficients $\alpha = 17$ and $\beta = C = 12$, respectively, the common slope (the strength gradient) at the inflection point and the same model parameters: $\bar{\sigma}_{m0} = 0.24$, $A = -4.7$ and $\dot{\varepsilon}_{0.5} = 1 \times 10^5\,\mathrm{s}^{-1}$.

(i) increasingly adiabatic deformation,
(ii) the resulting damage accumulation dominated by microcrack nucleation (as illustrated by Inset B of Figure 2), and
(iii) the reduction of aleatory variability of the system response.

This reduction of stochasticity is caused by the averaging effect of collective behavior of microcrack systems that smoothens the randomness at the macroscopic scale and by the diminishing flaw-sensitivity of brittle materials with the loading-rate increase [20]. Based on the results presented in Figure 2, the sigmoid tensile-strength model

$$(4.1) \qquad \bar{\sigma}_m = \frac{\sigma_m}{\sigma_m^{th}} = \bar{\sigma}_{m0} + (1 - \bar{\sigma}_{m0})\Big\{1 - \exp\Big[-\ln(2) \cdot \Big(\frac{\log(\dot{\varepsilon}) - A}{\log(\dot{\varepsilon}_{0.5}) - A}\Big)^C\Big]\Big\},$$
$$\log(\dot{\varepsilon}) \geqslant A$$

has been proposed in a normalized form to capture the mean tensile strength dependence on the strain rate [3, 27]. This phenomenological model is based on

the Weibull equation (2.7b) in conjunction with the translated Weibull cumulative distribution (2.1), which defines the fitting parameter

$$B = (\log \dot{\varepsilon}_{0.5} - A)(\ln(2))^{-1/C}$$

in terms of the strain rate $\dot{\varepsilon}_{0.5}$ by analogy with the median of the Weibull cumulative distribution (2.2). The independent variable (the strain rate) is, for convenience, presented in the format of the logarithm of base 10. The demonstrated disorder dependence of the strength increase [20] suggested that the process of activation and nucleation of micro-defects was governed substantially by the degree of structural heterogeneity of the quasibrittle system. The solid red curve in Figure 2 illustrates the effects of strain rate on the tensile strength of the quasi-brittle solids captured by the sigmoid transition (4.1) between the two limits

(4.2) $$\lim_{\dot{\varepsilon} \to 0}(\bar{\sigma}_m) = \bar{\sigma}_{m0}, \quad \lim_{\bar{\varepsilon} \to \infty}(\bar{\sigma}_m) = 1.$$

Both strain rate limits indicated in equation (4.2) deserve a careful scrutiny: (i) the upper strain rate bound is in reality finite and governed by Debye's atomic vibration period [28]; (ii) the lower strain rate bound (corresponding to the quasistatic loading) is, in terms of equation (4.2), identified with the translation (shift) parameter A. It is obvious from the standpoint of equation (4.1) that the quasistatic strength (σ_{m0}) is not truly a horizontal asymptote but rather the lower limit that is actually *reached* at $\log(\dot{\varepsilon}) = -A$. As suggested in [3], the notable advantage of equation (4.1) over the power-law empirical expression $\sigma_m = \sigma_{m0}\dot{\varepsilon}^m$ (typically used in the phenomenological constitutive laws that include rate dependency) is that it captures the high-strain-rate plateau ($\sigma_{m\infty}$) inferred by the shock experiments. The translation parameter, $A = -4.7$, and the sigmoidicity coefficient (the shape parameter), $\beta = 12$, of the Weibull model data fit (delineated in Figure 2 with the solid red line) are calculated iteratively by using equations (2.11b) and (2.12b) with values of the median, $\log(\dot{\varepsilon}_{0.5}) \approx 5.0$, and two symmetric quantiles, $\log(\dot{\varepsilon}_q) = \log(\dot{\varepsilon}_{0.4}) \approx 4.775$ and $\log(\dot{\varepsilon}_{1-q}) = \log(\dot{\varepsilon}_{0.6}) \approx 5.225$, estimated from the data plot (the full and open circles). In this case, the Weibull model fit is clearly superior to the Hill model fit (the dashed gray line) determined based on the same quantiles with the identical slope $\tilde{\sigma}'_m \approx 0.33$ calculated from equations (2.8).

The simplicity of equation (4.1) is remarkable. Experiments at only a few carefully selected strain rates may suffice to define, with reasonable confidence, the strength evolution within the entire strain rate range. At extreme loading powers (Region 3 in Figure 2), the upper-asymptote strength of quasibrittle systems is achieved through effective suppression of the cooperative phenomena, which drive the rapid strength increase in the transitional range (Region 2). Thus, the attainment of nearly theoretical strength (after practically linear stress-strain relationship up to catastrophic failure) and the disappearance of both intrinsic and extrinsic size effects at the extremely high loading rates are attributable to the strain rate-driven stochastic-to-deterministic transition of brittle response resulting from the diminishing role of microstructural disorder [3, 27]. On the other hand, at the low-to-medium loading powers (Region 1), the sample strength seems to be determined to a large extent by the stochastic distribution of intrinsic defects and more

sensitive to boundary conditions, since a few weak links (i.e., the microcracks thermally activated at the intrinsic defect locations) govern the catastrophic failure of the sample. These lattice-simulation observations are in agreement with the strain-rate sensitivity of small-scale metallic systems that is emerging recently. As an example, Greer and coworkers [29] reported that, at the relatively low strain rates (less than $0.1\,\mathrm{s}^{-1}$), the strength size dependence deviates from the ubiquitously observed power law.

4.1.2. *Dependence of the damage evolution and the representative sample size on the strain rate.* The monotonically increasing strength, captured by equation (4.1), has a typical sigmoid shape whose signatures are:

(i) relatively weak strain rate dependence at the two tail regions corresponding to the low-to-modest (Region 1 in Figure 2) and the ultra-high (Region 3) strain rates, and

(ii) strength surge, extremely steep and highly non-uniformly distributed over the strain-rate range.

This behavior is reflected qualitatively by the damage scaling exponent (δ) at the critical point, which is an informative damage parameter.

With reference to [3], the number of broken bonds that corresponds to the apex of the stress-strain curve (n_m) is determined for eight different lattice sizes (L) at seven different strain rates. The selected results presented in Figure 3 clearly indicate the gradual change of slope in the logarithmic (n_m vs. L) space. This observation suggests that a continuos spectrum of rate-dependent scaling exponents

$$(4.3) \qquad n_m \propto L^\delta, \quad \delta_0 = 1 < \delta = \hat{\delta}(\dot{\varepsilon}) < \delta_\infty = 2, \qquad \forall \dot{\varepsilon}$$

is necessary for the complete description of the two-dimensional system. Note that the critical value of the scalar damage parametar achieved at $t \equiv t_m \propto (\varepsilon_{cr}\dot{\varepsilon})^{-1}$ [27] is defined by $D_m = n_m/N \propto L^\delta$, where N designates the total number of bonds. The continuous spectrum of scaling exponents is, according to Figure 3, bounded by the inequality $(4.3)_2$.

The theoretical justification for the power-law behavior $(4.3)_1$ is not available at present. Nonetheless, it can be observed that in the dynamically-loaded brittle system, the δ value reflects the predominant distribution arrangement of the accumulated damage as depicted by the insets in Figures 2 and 4 illustrating the typical two-dimentional damage patterns. In fact, at smaller strain rates, as the failure pattern tends to a localized nearly-straight fracture, the exponent approaches the lower asymptote ($\delta_0 = 1$), whereas it increases progressively towards the upper asymptote ($\delta_\infty = 2$) as damaging becomes a more uniform process of microcrack nucleation extending over the entire lattice area for very high strain rates (Figure 3). The scaling exponent crossover

$$(4.4) \qquad \delta = 2 - \exp\left[-\ln(2)\cdot\left(\frac{\log(\dot{\varepsilon}) - A}{\log(\dot{\varepsilon}_{0.5}) - A}\right)^c\right], \qquad \log\dot{\varepsilon} \geqslant A$$

from the lower to the upper horizontal asymptote takes place primarily in the transitory region (Region 2) as indicated by Figure 4. The strain-rate sentitivity
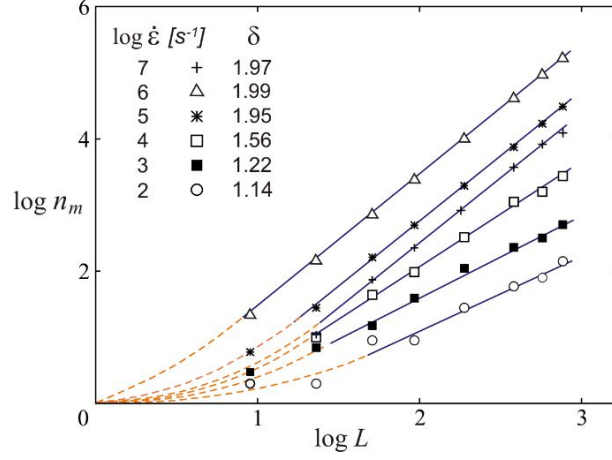
FIGURE 3. The change of the number of broken bonds correspond-
ing to the critical point with the size of square sample ($L \times L$) for
various strain rates. The straight lines represent the least-squares
data fit.

of the scaling exponent δ is closely related to that of the representative volume
element (RVE, see below).

The lattice size at which values of the stress-peak variables becomes size in-
dependent is defined herein as the representative sample and identified tentatively
with the RVE with respect to the tensile strength. The strain-rate governed de-
crease of the RVE, schematically depicted in Figure 4, appears qualitatively as a
mirror image, with respect to the abscissa, of the corresponsing strength increase
(Figure 2). The typical features include, once more, two regions of relatively mod-
est rate-sensitivity corresponding to loadings at the low and the very high strain
rates with a rapid decline towards the lower asymptote in the transitory region.
This pattern is represented qualitatively by the Weibull function:

$$(4.5)\quad \bar{L}_r = \frac{L_r}{L_{r0}} = 1 + (\bar{L}_{r\infty} - 1) \cdot \left\{ 1 - \exp\left[-\left(\frac{\log(\dot{\varepsilon}) - P}{R} \right)^Q \right] \right\}, \qquad \log(\dot{\varepsilon}) \geqslant P$$

where the RVE corresponding to quasistatic loading is designated as L_{r0}, and the
three uppercase alphabetic letters (P, Q, R) designate fitting parameters. Note the
transformation, L_r/L_{r0}, which leads to normalization of the ordinate on the plot
$\bar{L}_r = f(\dot{\varepsilon})$ illustrated in Figure 4.

The lower RVE asymptote ($L_{r\infty} \ll L_{r0}$), corresponding to the ordered ho-
mogeneous mesoscale damage patterns [16] at the theoretically maximum strain
rate [28], depends on the resolution length of the model l_c. It is defined at the
response-governing spatial scale that is individual for each material texture. Phys-
ically, it appears reasonable to suppose that for the high-quality ceramics, for
example titanium diboride or titanium carbide, $L_{r\infty}$ may be on submicrometer
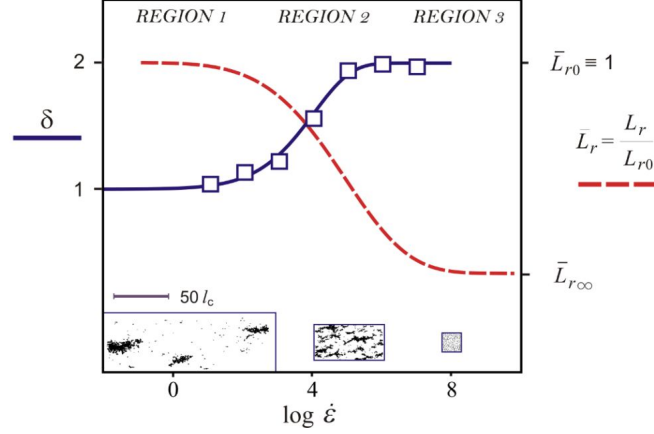scale. The typical damage patterns, associated in Figure 2 with the medium,

FIGURE 4. Sigmoid dependence of the damage scaling exponent (δ) at the critical point on the strain rate with square symbols depicting the simulation results and the solid blue curve the Weibull equation (4.4) fit with parameters $A = -10$, $C = 12$, and $\log(\dot{\varepsilon}_{0.5}) = 3.7$. The dashed red curve illustrates schematically the strain rate effect on the representative sample size (L_r).

transitory and extreme loading-rate ranges, provide graphical illustrations of the representative sample size rapid decline illustrated shematically in Figure 4 and captured qualitatively by equation (4.5). Since the present model cannot capture many significant physicochemical changes in material associated with high strain rates, these damage patterns are, necessarily, purely mechanical manifestations of the rate change reflected by the number and dynamic arrangements of broken bonds. Nonetheless, the reduction of L_r is physically sound bearing in mind the previosly-noted diminishing role of microstructural disorder.

4.2. High-Velocity Expansion of a Cylindrical Cavity. Dynamic expansion of a cylindrical cavity is a problem important to several fields of engineering [30]. The study presented herein was motivated by the high-velocity penetration of rigid projectiles through materials with inferior cohesive strength [23, 31]. The simulation setup was simple. The cavity was nucleated by removal of a single particle from the middle of the random particle network of circular shape. The nearest neighbors of the removed particle defined the cavity rim, which was driven radially outward in a displacement-controlled manner at a desired constant expansion rate $\dot{a}$ (the inset in Figure 5a). The computation domain representing a plane with an expanding cavity in its center was divided into five annular regions of equal width over which the macroscopic field observables were averaged by using equations (3.1) and (3.2). The averaging regions were marked with five upper case Gothic letters ($\mathfrak{A}$–$\mathfrak{E}$) starting from the one closest to the expanding cavity rim as indicated in the inset of Figure 5a. The scalar damage parameter was again defined as the ratio of the number of broken bonds with the total number of bonds

$(D = n/N)$. Additionally, the effect of damage accumulation was quantified by calculation of the effective stiffness components that took into account material degradation.

4.2.1. *Damage accumulation and degradation of the effective material properties.* The selected simulation data obtained for the high cavity expansion rate $\dot{a} = 0.135\,C_0$ are presented in Figure 5 by the hollow squares and circles corresponding, respectively, to the two averaging regions $\mathfrak{A}$ and $\mathfrak{B}$ closest to the expanding cavity rim. The history of the scalar damage parameter D is of the typical sigmoid shape bracketed by two horizontal asymptotes depicting the initially undamaged (pristine) state and the final damage (completely pulverized) state of the sample, respectively. As discussed in [23], the effective circumferential stiffness degrades more rapidly than the radial stiffness since initially most of the damage in the process zone is attributable to the radial microcracks. Also, the degradation rate of the effective radial stiffness depends on the radial distance from the cavity, while the degradation rate of its circumferential counterpart is insensitive appearently to the radial coordinate. Since initially most of the damage in the process zone (the one closest to the expanding cavity rim) is attributable to the radial microcracks, the circumferential stiffness degrades much more rapidly then the radial stiffness. These effects are obliterated in the damage evolution plots presented in Figure 5a due to the spherical (non-directional) character of the scalar damage parameter.

The sigmoid character of the damage evolution depicted by the simulation data points is represented by the Hill model (2.7a) as follows

$$(4.6) \qquad D = \frac{(t - T)^\alpha}{(t_{0.5} - T)^\alpha + (t - T)^\alpha}, \qquad \alpha > 0, \ t \geqslant T.$$

By analogy with the original Hill model, minimum ($D_0 \equiv 0$) and maximum effects ($D_1 \equiv 1$) appear implicitely in equation (4.6), $t_{0.5}$ is the time corresponding to $D = 0.5$, while the shape parameter α represent the coefficient of sigmoidicity.

The damage evolution expression (4.6) can be linearized by using logarithmic transformations

$$(4.7) \qquad \begin{aligned} \ln\left(\frac{D}{1 - D}\right) &= \alpha \ln(t - T) - \alpha \ln(t_{0.5} - T) \\ \log\left(\frac{D}{1 - D}\right) &= \alpha \log(t - T) - \alpha \log(t_{0.5} - T) \end{aligned}$$

with two different logarithm bases. Equation (4.7), known as the median-effect equation, permits estimation of the median ($t_{0.5}$) and the slope (α) of simulation data by one of the regression methods. Interestingly, this equation is mathematically identical to the logit transformation, $\mathrm{logit}(p) = \ln(p/1 - p)$ [6][3]

Importantly, the final saturation state of the scalar (spherical) damage parameter is known by definition ($D_1 \equiv 1$). Thus, it is especially convenient to use the quantiles for the estimation of the shape (2.11a) and location (2.12a) parametes

---

[3]The logit of the probability $p = P\{X \leqslant x\}$ of the event $\{X \leqslant x\}$ is defined as the logarithm of the corresponding odds $p/(1 - p)$, which yields the Hill equation (2.7a) in a linear form $\mathrm{logit}(p) = \alpha \ln[(x - A)] - \alpha \ln(x_{0.5} - A)$.
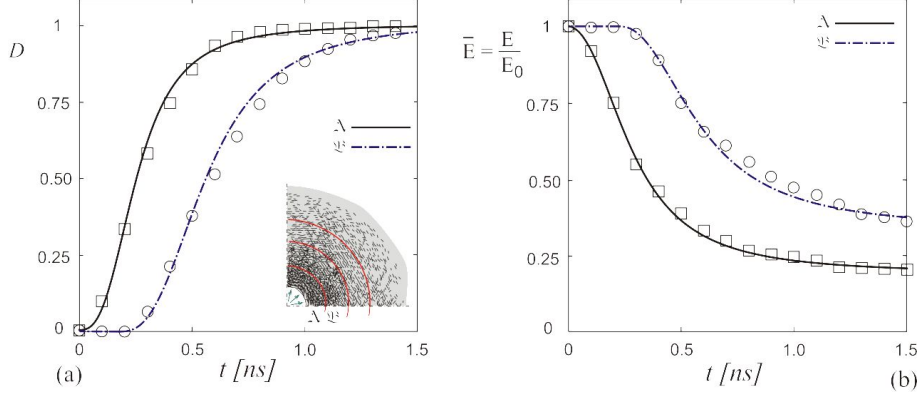
FIGURE 5. Time history of: (a) scalar damage parameter, and (b) effective modulus of elasticity in annular regions A and B, which illustrate the material degradation in the process zone due to microcrack nucleation for the high cavity expansion rate 0.135 C_0. The data fitting curves are plotted, for the two annular regions indicated in the inset, by using the equations (4.6) and (4.8) with the coefficients of sigmoidicity being, respectively: (a) $\alpha = (2.9,\ 2.7)$ and (b) $\alpha = (-2.4;\ -2.2)$, while the parameters $T = (0,\ 0.2)$ and $t_{0.5} = (0.26,\ 0.59)$ are common for both macroscopic observables and $E_1 = (0.20,\ 0.35)$.

if the damage evolution process has not approached the saturation level. Thus, the two data fitting curves illustrated by the solid and dash-dotted lines in the main pannel of Figure 5a are plotted by using equation (4.6) with the parameters $\alpha = (2.9, 2.7)$, $T = (0,\ 0.2)$ and $t_{0.5} = (0.26,\ 0.59)$ corresponding to the two averaging regions $(\mathfrak{A}, \mathfrak{B})$, respectively.

These model parameters are calculated based on the medium and two symmetric quantile values estimated from the simulation data to be $t_{0.5} = (0.26,\ 0.56)$, $t_q = t_{0.4} = (0.22,\ 0.51)$, and $t_{1-q} = t_{0.6} = (0.29,\ 0.62)$ for the two averaging regions $(\mathfrak{A}, \mathfrak{B})$, respectively.

The simulation data points in Figure 5b suggest that the damage-induced reduction of the effective modulus of elasticity (3.2) follows a reverse-sigmoid shape. Therefore, a descriptive model

$$(4.8) \qquad \bar{E} = \frac{E}{E_0} = \bar{E}_1 + (1 - \bar{E}_1)\frac{(t-T)^\alpha}{(t_{0.5}-T)^\alpha + (t-T)^\alpha}, \qquad \alpha < 0,\ t \geqslant T$$

based on the Hill equation (2.7a) with a negative coefficient of sigmoidicity α is used herein to capture the characteristic monotonic decline depicted in Figure 5b by squares and circles referring to the pair of circular averaging regions $(\mathfrak{A}, \mathfrak{B})$. It should be noted that the final saturation level (corresponding to the damage parameter approaching $D_1 \equiv 1$) is not zero due the fact that the lattice model used, in addition to a chemical, recognizes also a purely mechanical interaction

between particles. The former is inherently both compressive and tensile while the later is strictly compressive (but with unlimitted number of particles potentially involved). Namely, the mechanical interaction can be established between two particles that were not initially connected or re-established between particles that were previously separated by the (chemical) bond rupture. This interaction feature is essential for modeling of the flow of the comminuted phase in the process zone during cavity expansion. Thus, the non-zero modulus of elasticity corresponding to the comminuted material ($D_1 \equiv 1$) is apparent since the tension carying capacity is reduced to zero.

4.3. Impact Fragmentation of a Slender Nanoprojectile. The Weibull probability distribution (2.1) is used extensively to describe particle size distribution in comminution process (e.g., [5]). Thus, the extension to the description of the maximum fragment mass of a projectile colliding with a rigid wall is natural and straightforward. This, so called, ballistic Taylor experiment, is a standard procedure for verification of constitutive behavior of materials [32]. In the studies reviewed herein, the slender L-J nanoprojectile (the aspect ratio of ≈ 7.3) impacted a rough rigid target represented by a line of immovable atoms. Depending of the striking velocity, the collision resulted in more or less severe plastic distortion of the projectile until the impact energy exceeded the absorption capacity of the material, which resulted in creation and energetic evacuation of fragments. These MD simulations generated information at the atomic level which could be converted into macroscopic observables (temperature, $\mathcal{T}$; pressure, $\mathcal{P}$; and strain, ε) by well-known techniques presented in an abbreviated form in Section 3.1 of this review article. The distribution of fragment masses was also evaluated periodically during the impact as the surviving interatomic links defined self-bounding clusters of atoms with interatomic distance less that a predetermined cut-off limit ($r \leqslant R_{lim}$).

4.3.1. *Dependence on the maximum fragment mass on the selected macroscopic observables.* With impact energy, $\mathcal{K} = mv^2/2$, as a control parameter, the reverse-sigmoid dependence of the maximum fragment mass ($m_{\max}$) upon a set of macroscopic observables denoted by a generic state variable $\Xi \in \{\mathcal{K}, \mathcal{P}_{\max}, \mathcal{T}_{\max}, \dot{\varepsilon}_{\max}\}$ for the *entire* fragmentation range is schematically depicted by the following expression

$$
(4.9) \qquad \ln m_{\max} = M_0 \cdot \exp\Big[- \Big(\frac{\ln \Xi - Z}{Y}\Big)^X \Big], \qquad (\Xi \geqslant \Xi_0)
$$
$$
M_0 = \frac{Y}{X} \cdot \exp\Big(1 - \frac{1}{X}\Big) \cdot \xi
$$

and illustrated by Figure 6 [12]. The phenomenological model (4.9) is developed based on the reverse-sigmoid form of the Weibull equation (1.1b), where the three uppercase alphabetic letters (X, Y, Z), as in the preceding cases, designate the fitting parameters (for example, in Figure 6a, $X = 4$, $Y = 7$, $Z = 2.2$). The parameters $(\Xi_0, m_{\max 0})$, designated by subscript "0", refer to the threshold of the damage-fragmentation transition as illustrated in Figure 6. The damage-fragmentation transition is a continuous phase transition discussed extensively over the last 15 years (e.g., [33] and references therein). For a slender projectile of any given aspect ratio, the onset of the damage-fragmentation transition is dependent upon

its cross sectional dimension. The nonlinear empirical formula (4.9) neglects the minuscule fragmentation below the onset of the damage-fragmentation transition ($v < v_0$; $\Xi < \Xi_0$; Figure 6). (The impact fragmentation in confined spatial dimensions is expected to result in increased fragmentation thresholds due to the small-scale hardening of the material as indicated, for example, by Rinaldi [34].)

It should be obvious from expression (4.9) and upon a closer inspection of Figure 6 that the three fitting parameters (X, Y, Z) are not mutually independent but need to satisfy the following condition from the approximately linear domain

$$(4.10) \qquad \xi = \ln m_{\max 0} \cdot \frac{X}{Y} \cdot \exp\Big[-1 + \frac{1}{X} + \Big(\frac{\ln \Xi_0 - Z}{Y}\Big)^X \Big],$$

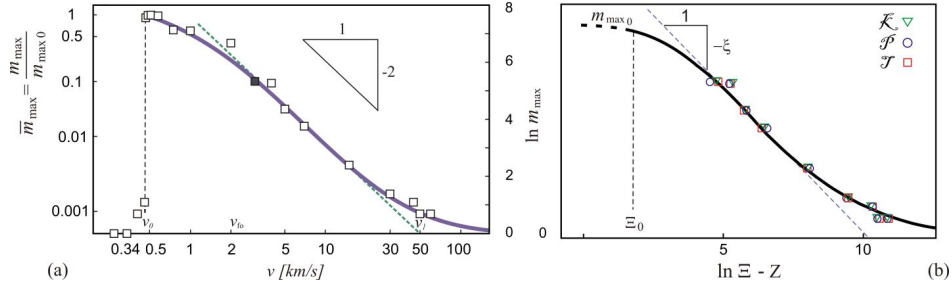$$\ln \Xi_\xi = Z + Y\Big(1 - \frac{1}{X}\Big)^{1/X}$$

FIGURE 6. (a) The normalized maximum fragment mass vs. the striking velocity with square symbols depicting the MD simulation data and the solid curve the data fit with Equation (4.9). (b) Schematics of the maximum fragment mass dependence on a generic state variable $\Xi \in \{\mathcal{K}, \mathcal{P}_{\max}, \mathcal{T}_{\max}, \dot{\varepsilon}^2\}$. The results correspond to $\bar{d} = 53$ ($15 \times 110\,\text{nm}$). (The projectile diameters are presented henceforth in nondimensional form by normalization with the equilibrium interatomic distance, $\bar{d} = d/r_0$.

The slope at the inflection point $(4.10)_1$ is uniquely determined from the condition that it corresponds to the second derivative of (4.9) being equal zero.

The empirical expression (4.9) cannot formally capture the terminal (shattering) fragmentation, $v = v_1 \leftrightarrow m_{\max} \equiv 1$, except as the limit case, $\lim_{\Xi \to \infty}(m_{\max}) = 1$, defining the horizontal asymptote depicted schematically by abscissa in Figure 6b. (It should not be overlooked that simulation data presented in Figure 7 depicts the terminal fragmentation[4] obtained, not-surprisingly, for the smallest projectile diameter used in the investigation ($\bar{d} = 19$).

---

[4]The terminal or "shattering" phase transition (with the onset $v \equiv v_1$) is defined by occurrence of the uniformly monatomic fragment debris ($m_{\max} \equiv 1$) accounting for a deterministic fragment distribution. The term "shattering" is inspired by Redner's [35] discussion of a mathematical patohlogy in a solution of the linear fragmentation rate equations "in which mass is lost to a dust phase consisting of an infinite number of zero mass particles".

Furthermore, the simulation-data fitting by (4.9) reveals not only that the fitting parameters X and Y have the same values for all four impact parameters and state variables $\Xi \in \{\mathcal{K}, \mathcal{P}_{\max}, \mathcal{T}_{\max}, \dot{\varepsilon}_{\max}^2\}$ but also that

$$X \approx 2\xi, \quad Y \approx \ln m_{\max 0}$$

Thus, equation (4.9) can be rewritten in a more visually appealing form

$$(4.11) \qquad \ln m_{\max} = \ln m_{\max 0} \cdot \exp\left[1 + \ln\frac{1}{2} - \frac{1}{2\xi} - \left(\frac{\ln \Xi - Z}{\ln m_{\max 0}}\right)^{2\xi}\right]$$

Consequently, the nonlinear phenomenological model for the maximum fragment mass is captured by the same reverse-sigmoid curve for all four above-mentioned state parameters when the independent generic variable, $\ln \Xi$, is shifted by Z (4.11) as illustrated in Figure 6b and discussed in [12].

Finally, the size effect of the damage-fragmentation transition threshold observed in the ballistic Taylor experiments investigated in [11] is extended in this review article to include the maximum fragment mass (absolute rather than commonly-used normalized counterpart). Timar et al. [33] assumed the scaling form for the critical striking velocity

$$(4.12) \qquad\qquad v_0(d) = v_0(\infty) + A\bar{d}^{-1/\upsilon}, \qquad \bar{d} \geqslant \bar{d}_L$$

in terms of the system size. The limit of validity of the power law (4.12) for the impact fragmentation of slender projectiles was proposed based on observation that in the small-size region ($\bar{d} < \bar{d}_L \approx 29$) the critical striking velocity deviates from (4.12) by becoming insensitive to the projectile diameter [11]. The critical striking velocity of the infinite system and the correlation length exponent of the transition $(4.12)_1$ were identified to be $v_0(\infty) = 0.40\,\text{km/s}$ and $\nu = 0.77 \pm 0.01$, respectively [11].

With regards to results of the trailblazing study of Kun and Herrmann [36] it can be assumed that: (i) the system exhibits a continuous phase transition at the damage-fragmentation threshold $(v_0, m_{\max 0})$), (ii) the maximum fragment mass is the order parameter of that transition, and (iii) the striking velocity (v) is the control parameter of that transition. The finite size scaling of the maximum fragment mass (Figure 7a) could be admitted in the form

$$(4.13) \qquad\qquad \ln m_{\max}(v, \bar{d}) = \bar{d}^{-\beta/\nu} F\{[v(\bar{d}) - v_0(\infty)]\bar{d}^{1/\nu}\}$$

where β is the critical exponent of the order parameter and F designates the scaling function (e.g., [33, 38]) illustrated by reverse-sigmoid curves of Figure 7a. Thus, Figure 7b is obtained by rescaling v (4.12) and $m_{\max}$ (4.13) by appropriate powers of the projectile diameter defined by scaling exponents $\nu = 0.77 \pm 0.01$ and $\beta = -0.25 \pm 0.02$. These exponents are identified from simulation results based on the transition-point data collapse requirement. Figure 7b illustrates that collapse of the $m_{\max} = \hat{m}_{\max}(v_i)$ curves for $\bar{d} \in \{33, 45, 53\}$. The detailed view of the critical-point neighborhood, presented as inset in Figure 7b, emphasizes both the good-quality data collapse of these curves at the transition threshold for the three selected projectile diameters $\bar{d} \geqslant \bar{d}_L$ as well as the horizontal peak shift of the curve belonging to the small-size plateau $\bar{d} = 19 < \bar{d}_L$. These observations resemble
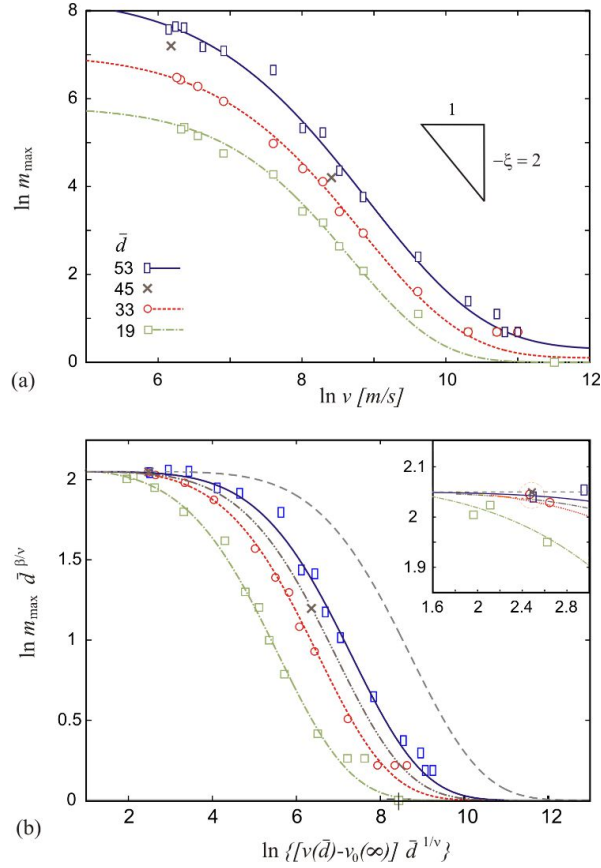
FIGURE 7. (a) Logarithmic plot of the maximum fragment mass (m_{max}) vs. the striking velocity (v) with symbols depicting the MD simulation results for four different projectile diameters and curves the corresponding data fits with equation (4.9). (b) Scaled logarithmic $m_{\max} = \hat{m}_{\max}(v, \bar{d})$ curves of Figure 7a corresponding to the transition threshold $(v_0, m_{\max 0})$ collapse for the three projectile diameters $\bar{d} \in \{33, 45, 53\}$ belonging to the power-law (4.12) validity range. Inset: A detail of the main plot emphasizing the neighborhood of the onset on the damage-fragmentation phase transition; the data points for $\bar{d} = 19$ are added to highlight the horizontal peak shift of the curves belonging to the small size plateau. (All projectiles have the same slenderness ratio.)

those already reported for the similar scaling of the average fragment mass [11] in agreement with the claim of Kraft et al. [37] that "there is no scaling law with one universal power-law exponent encompassing the entire size-dependent range (of the mechanical strength)". It cannot be overemphasized that all curves in Figure 7b

are fitted with the Weibull-type function (4.9) with all fitting parameters identical with exception, naturally, of the location parameter Z. Therefore, shifting of the curves would result in their overlap in the linear transition region similar to that illustrated in Figure 6b.

In addition to obvious usefulness of the scaling approach (4.12), (4.13) as a simple but powerful conceptual analytical tool [38], the set of reverse-sigmoid curves in Figure 7b offers a number of visual benefits for the analysis of the impact fragmentation of slender projectiles. First, it is straightforward to both interpolate (the dash-double-dot gray line in Figure 7b) and extrapolate (the dashed gray line) simulation results with a minimum additional computational effort. Second, the coordinates of the transition threshold $(v_0, m_{\max 0})$ are defined for every system size. Third, it is possible to estimate the terminal velocity, $v_1(\bar{d})$, by introducing an abscissa neighborhood of predetermined thickness to Figure 7b and determine its interception with the particular $\bar{d}$ curve (fit). As an example, for $\bar{d} = 53$, the terminal velocity could be pinpointed roughly to $v_1 \approx 250 \pm 20\,\text{km/s}$ with the lower-horizontal-asymptote (i.e., abscissa) neighborhood thickness set arbitrarily to 5 percent of the biatomic fragment ($m_{max} = 2$) vertical coordinate. (The thickness of this barely-visible gray stripe along the abscissa in Figure 7b is selected based on the available terminal fragmentation datum for $\bar{d} = 19$.) This, although admittedly a rather arbitrary and coarse estimate, not-surprisingly exceeds the linear-model prediction of $45\,\text{km/s}$ quite substantially (Figure 6a) [10]. Note that the later linear-model prediction was already proven to underestimate v_1 by a hefty margin since the terminal fragmentation for $\bar{d} = 53$ have not been achieved in MD simulations even at $v = 60\,\text{km/s}$ [12]. As a final note, it seems reasonable to assume that, within the framework of the present analysis, there is a *saturation* system size (defining the limiting curve) beyond which the terminal fragmentation is impossible to ahieve.

5. Summary

The sigmoid and reverse-sigmoid response patterns reviewed herein were observed lately in the analyses of simulation data obtained by two different methods of the computational mechanics of discontinua: molecular dynamics and lattice. Two functional models, referred herein as the Hill model and the Weibull model, were suggested as useful tools not only for data fitting but also for investigation of the salient features of the simulated phenomena. The sigmoid (the reverse-sigmoid) response patterns were characterized by two horizontal asymptotes at the domain tails, which bound the regions of relatively weak dependence of the dependent variable upon the independent one, and a smooth comparably-steep transition in between with a non-negative (a non-positive) derivative at each point for the two respective shapes. The gradient of this transition, as a rule, has a very important physical meaning for the material response modeling. The various properties of the Hill and Weibull models, used frequently as curve fitting tools for nonlinear and saturable phenomena, were reviewed with emphasis on the parameters governing the essential response features. Although the satisfactory curve-fitting of data does not imply causality, it might, hopefully, hint at a future investigation

pathway. It should be noted that the physical mechanisms, which the described-patterns embody, are still not understood fully. That is, outlooks of the purely empirical functions of various physical parameters are not sufficiently clear. Therefore, in absence of the complete physical picture and derivations from the first principles, the expressions presented strive at best to formal significance common to all phenomenological models and empirical formulas manufactured to capture experimental data or simulation results.

References

1. D. Krajcinovic, *Damage Mechanics*, Elsevier, 1996.
2. S. Mastilovic, *Further remarks on stochastic damage evolution of brittle solids under dynamic tensile loading*, Int. J. Damage Mech. **20** (2011), 900–921.
3. S. Mastilovic, *On strain-rate sensitivity and size effect of quasi-brittle solids: Transition from cooperative phenomena to microcrack nucleation*, Contin. Mech. Thermodyn. **25** (2013), 489–501.
4. H. Rinne, *The Weibull Distribution, A Handbook*, CRC Press, 2008.
5. P. Rosin, E. Rammler, *The laws governing the fineness of powdered coal*, J. Institute of Fuel **7** (1933), 29–36.
6. S. Goutelle, M. Maurin, F. Rougier, X. Barbaut, L. Bourguignon, M. Ducher, P. Maire, *The Hill equation: A review of its capabilities in pharmacological modeling*, Fundamental and Clinical Pharmacology **22** (2008), 633–648.
7. A. V. Hill, *The possible effects of the aggregation of the molecules of haemoglobin on its dissociation curves*, J. Physiol. **40** (1910), iv–vii.
8. A. Rinaldi, S. Mastilovic, *Two-Dimensional Discrete Damage Models: Lattices and Rational Models*, in *Handbook of Damage Mechanics: Nano to Macro Scale for Materials and Structures* (ed. G. Voyiadjis), Springer, Germany, 305–338, 2014.
9. B. Leimkuhler, C. Matthews, *Molecular Dynamics: With Deterministic and Stochastic Numerical Methods*, Springer, 2015.
10. S. Mastilovic, *Impact fragmentation of nanoscale projectiles at ultrahigh striking velocities*, Meccanica **50** (2015), 2353–2367.
11. S. Mastilovic, *Molecular-dynamics simulations of the nanoscale Taylor test under extreme loading conditions*, Math. Mech. Solids **21**(3) (2016), 326–338.
12. S. Mastilovic, *Phenomenology of the maximum fragment mass dependence upon ballistic impact parameters*, Lat. Am. J. Solids Struct. **14** (2017), 1529–1546.
13. M. P. Allen, D. J. Tildesley, *Computer Simulation of Liquids*, Oxford University Press, 1996.
14. L. Verlet, *Computer "experiments" on classical fluids. I. thermodynamics properties of Lennard–Jones molecules*, Phys. Rev. **159**(1) (1967), 98–103.
15. M. Zhou, *A new look at the atomic level virial stress: on continuum-molecular system equivalence*, Proc. R. Soc. Lond., A, Math. Phys. Eng. Sci. **459** (2003), 2347–2392.
16. S. Mastilovic, *A note on short-time response of two-dimensional lattices during dynamic loading*, Int. J. Damage Mech. **17** (2008), 357–361.
17. M. J. Buehler, *Atomistic Modeling of Materials Failure*, Springer, 2008.
18. B. L. Holian, A. F. Voter, R. Ravelo, *Thermostatted molecular dynamics: how to avoid the Tada demon hidden in Nose–Hoover dynamics*, Phys. Rev. E **52** (1995), 2338–2347.
19. D. J. Fung, *A First Course in Continuum Mechanics*, Prentice Hall, 1994.
20. S. Mastilovic, A. Rinaldi, D. Krajcinovic, *Ordering effect of kinetic energy on dynamic deformation of brittle solids*, Mech. Mater. **40**(4–5) (2008), 407–417.
21. J. H. Weiner, *Statistical Mechanics of Elasticity*, 2nd ed., John Wiley & Sons, 2002.
22. B. Lawn, *Fracture of Brittle Solids*, 2nd ed., Cambridge University Press, 1993.
23. S. Mastilovic, D. Krajcinovic, *High velocity expansion of a cavity within a brittle material*, J. Mech. Phys. Solids **47** (1999), 577–610
24. J. Lubliner, *Plasticity Theory*, Macmillan, 1990.

25. B. L. Holian, D. E. Grady, *Fragmentation by molecular dynamics: the microscopic "big bang"*, Phys. Rev. Lett. **60** (1988), 1355–1358.

26. S. Nemat-Nasser, M. Hori, *Micromechanics: Overall Properties of Heterogeneous Materials*, North-Holland, 1999.

27. S. Mastilovic, *Some observations regarding stochasticity of dynamic response od 2D disordered brittle lattices*, Int. J. Damage Mech. **20** (2011), 267–277.

28. C. Qi, M. Wang, Q. Qian, *Strain rate effects on the strength and fragmentation size of rocks*, Int. J. Impact Eng. **36** (2009), 1355–1364.

29. A. T. Jennings, J. Li, J. R. Greer, *Emergence of strain-rate sensitivity in Cu nanopillars: Transition from dislocation multiplication to dislocation nucleation*, Acta Mater. **59** (2011), 5627–5637.

30. H. G. Hopkins, *Dynamic expansion of spherical cavities in metals*, in: *Progress in Solid Mechanics* (Editors I. N. Sneddon, R. Hill), **1**, 83–163. North-Holland, The Netherlands, 1960.

31. S. Mastilovic, D. Krajcinovic, *Penetration of Rigid Projectiles Through Quasi-Brittle Materials*, J. Appl. Mech. **66** (1999), 585-592.

32. M. A. Mayers, *Dynamic Behavior of Materials*, John Wiley, 1994.

33. G. Timár, F. Kun, H. A. Carmona, H. J. Herrmann, *Scaling laws for impact fragmentation of spherical solids*, Phys. Rev. E **86**(4) (2012), 016113.

34. A. Rinaldi, *Effects of dislocation density and sample size on plastic yielding at the nanoscale: a Weibull-like framework*, Nanoscale **3**(1) (2011), 4817–4823.

35. S. Redner, *Fragmentation*, in: *Statistical Models for the Fracture of Disordered Media* (Eds. H. J. Herrmann, S. Roux), North-Holland, 321–348, 1990.

36. F. Kun, H. J. Herrmann, *Transition from damage to fragmentation in collision of solids*, Phys. Rev. E **59**(3) (1999), 2623–2632.

37. O. Kraft, P. A. Gruber, R. Monig, D. Weygand, *Plasticity in confined dimensions*, Annual Rev. Mater. Research **40** (2010), 293–317.

38. D. Stauffer, A. Aharoni, *Introduction to Percolation Theory*, Taylor & Francis, 1992.

НЕКИ СИГМОИДНИ И ОБРНУТО-СИГМОИДНИ ОБРАСЦИ ОДЗИВА СОЛИДА КОЈИ СЕ ЈАВЉАЈУ ПРИ ИЗУЗЕТНО СНАЖНИМ ОПТЕРЕЋЕЊИМА

РЕЗИМЕ. Циљ овог прегледног рада је двострук. Прво, да истакне неке сигмоидне и обрнуто сигмоидне обрасце одзива примећене у скорије време приликом симулација оптерећења (углавном, квазикртих) солида великим брзинама деформисања. Друго, да прикаже различите особине два модела који се често користе као алати за "фитовање" кривих код нелинеарних појава које карактерише засићење. Ова два модела - инспирисана Хиловом и Вејбуловом функцијом расподеле вероватноћа - ограничена су двема хоризонталним асимптотама са глатким прелазом између основног и коначног стања засићења који одликују не-негативни (не-позитивни) први изводи у свакој тачки сигмоидног (обрнуто сигмоидног) облика. Мада се користе пре свега за "фитовање" података због своје флексибилности и ефикасности, ови нелинеарни модели поседују и друге одлике погодне при анализи неповратних, нелинеарних и неравнотежних појава. Особине ова два модела су у овоме прегледу систематски изложене. Упркос чињеници да се успешно "фитовање" података не може сматрати доказом узрочности, оно би могло да истакне образац понашања и, можда, пружи смернице за даља истраживања.

Институт за мултидисциплинарна истраживања

Универзитет у Београду

Београд

Србија

misko.mastilovic@imsi.bg.ac.rs